Gauge Dynamics In Numerical Relativity

Integrated M.Sc. Thesis

Submitted to

CENTRE *for* EXCELLENCE IN BASIC SCIENCES

Department of Atomic Energy
University of Mumbai, Kalina campus
Mumbai - 400098, India

Author:
S. Vivekanandji Chaurasia
Roll No:
P011506

Advisor:
Prof. Mark Hannam
Gravitational group
Cardiff University

Co-advisor:
Prof. P.Ajith
Astrorelativity group
ICTS-TIFR

External Examiner's Signature:

Thesis Guide's Signature:

Abstract

Numerical solutions of Einstein's equations for black-hole-binary systems play an important role in attempts to observe and measure gravitational waves. The most popular and robust approach to do this is the "moving puncture method", which is based on the ADM-BSSN decomposition of Einstein's equations. The computational cost and efficiency of such codes is dominated by the numerical resolution required near the black hole. Given the coordinate freedom of general relativity, we can in principle change the coordinate size of the black holes, and thus relax these resolution requirements. In this work we explore one approach to do that, where the standard moving-puncture gauge conditions are modified to introduce a component to the "shift vector", which adjusts the coordinates in the vicinity of the black hole and "stretches" the horizon. We find that we are able to rescale the coordinate size of the Schwarzschild black hole considered in this work. Closer analysis of constraint violations reveals that the constraints do not converge to zero, suggesting an inconsistency somewhere in the implementation of the method. The current work suggests that the method holds promise, once these inconsistencies are corrected.

Acknowledgements

First of all, I would like to thank my advisor Mark Hannam for finding this very interesting topic and giving me the opportunity to write this thesis in his group. I also thank my co-advisor P.Ajith for his guidance and support during my term as a project student.

Gravitational group members in Cardiff University and ICTS-TIFR, especially Sebastian Khan, Alex Vano-Vinuales, Nathan Johnson-McDaniel (ICTS), and Paul Hopkins deserve many thanks for their helpful discussions, technical help and for making it a pleasure to spend time in the office.

Last but not least, I want to thank my friends and my parents who have always given me their support and encouragement, for which I am grateful.

Statement of Authorship

Herewith, I certify that this thesis has been composed by myself and describes my own work unless otherwise acknowledged in the text. I created all figures on my own unless explicitly referred to the source. Parts that are direct quotes or paraphrases are identified as such.

Cardiff, November 14, 2015 $\overline{(Swami\ Vivekanandji\ Chaurasia)}$

Contents

Chapter 1

Introduction

The theory of general relativity forms the foundation of our understanding of modern cosmology, the physics of neutron stars and black holes, the generation of gravitational radiation, and any other cosmic phenomena in which strong-field gravitation plays a dominant role.

The theory itself has never been tested except in the weak-field, slow velocity regime. Solutions to Einstein's equations have not been explored in much detail except for analytical solutions with a high degree of symmetry. Solutions that lack symmetry are difficult to work out analytically, and in most cases not even possible. Also, most of the dynamical scenarios thought to occur in nature lack any symmetry and so one has to solve Einstein's equations numerically. With the advancement in computing technology, it is now possible to tackle these complicated equations numerically and explore these scenarios in detail. This is the main goal of numerical relativity.

Starting this year, a number of gravitational wave detectors will go on-line, allowing the observation of gravitational radiation for the first time[2]. One class of events which is expected to produce detectable radiation is the coalescence of two black holes. For distinguishing such an event from others, and interpreting the data from such an event, it will be important to calculate the parameters of the waveform for collisions between two black holes[3]. To produce those waveforms, it will be necessary to solve Einstein's equations for the relevant physical situations.

The field equations are a set of coupled, nonlinear, partial differential equations. There is no analytic solution for the problem of two black holes in orbit. In general, perturbation theory is not

applicable, due to the strong gravitational fields involved[1]. Therefore, the problem must be solved numerically. In doing so one soon finds that solving Einstein's equations numerically for even a spherical, stationary black hole is a challenging problem in itself.

Numerical Relativity being a vast subject, in this thesis we partially explore the gauge or the coordinate freedom in solving Einstein's equations. In particular we want to improve the accuracy and efficiency of the existing simulations and want to understand how to be able to control the gauge dynamics in numerical simulations. Our approach is based on being able to control the size of the black holes apparent horizon. Being able to do so will allow one to make the simulations faster. This can be seen from the *Courant* relation $dt \leq \frac{1}{2}dx$, where dt is the time resolution and dx is the grid resolution.

1.1 Organization

This thesis is organized as follows: in Chapter 2 we describe the theoretical framework for the numerical evolution of the Einstein's equations. We start with a short note on general relativity in Section 2.1 and then in Section 2.2 motivate why we need accurate and efficient numerical spacetimes by showing order of magnitude estimate for gravitational waves that are generated in cataclysmic events such as coalescence of two black holes, which the numerical spacetimes simulate. In Section 2.3 we present a brief derivation of the 3+1 decomposition (ADM formalism) of Einstein's equation that form the basis for solving the field equations on a computer. In Section 2.4 we summarize the modified form of the ADM formalism, namely the BSSN-formalism which is the workhorse for stable evolution of the field equations. We then give a brief introduction to obtaining initial data for the specific system to be evolved in Section 2.5. 'Good' choice of the gauge (coordinates) for stable numerical evolution of Einstein's equation is important. We present a short note on this in Section 2.6 and the particular choice we used in this thesis. Section 2.7 show the convergence results from the evolution of the discretized field equations (BAM code).

In Chapter 3 we introduce the concept of apparent horizon which is an important diagnostic tool

[1] Perturbation theory can be used to describe the ringdown.

used during numerical evolutions. In Section 3.1 we give an introduction to trapped surfaces in GR and derive the equation for the apparent horizon. We briefly describe how apparent horizons are located on a numerical grid in Section 3.2 mainly focusing on 'Flow'-algorithm that the BAM code uses. We present the modification to the BAM code in Section 3.3, particularly presenting the idea that we are trying to pursue for 'shifting' the horizon in order to to control the coordinate size of a black hole. We present the results that we have obtained so far in Section 3.4.

1.2 Notation and Conventions

Throughout this thesis, we will use the unit convention that the gravitational constant G and the speed of light c are unity unless stated otherwise. Greek indices and Latin indices $a-h$ and $o-z$ are taken to run from 0 to 3, and Latin indices $i-n$ from 1 to 3. The metric signature used is (- + + +).

Partial derivatives with respect to a coordinate x^i will be indicated with the symbol ∂_i. Covariant differentiation with respect to a coordinate x^a on a 4-dimensional spacetime will be indicated with the symbol ∇_a , and covariant differentiation with respect to a coordinate x^i on 3-dimensional slices will be indicated with the symbol D_i . Lie differentiation with respect to a vector field n^a will be indicated with the symbol $\mathcal{L}_{\mathbf{n}}$.

Chapter 2

Numerical Spacetimes

2.1 Reviewing General Relativity

The field equations of general relativity relate the geometry of spacetime with its matter and energy content. Written in index notation they state:

$$G_{ab} = R_{ab} - \frac{1}{2} g_{ab} R = 8\pi T_{ab} \tag{2.1}$$

where g_{ab} is the metric tensor, R_{ab} is the Ricci tensor, R is the Ricci scalar, T_{ab} is the energy-momentum tensor and the Einstein tensor G_{ab} is a nonlinear differential operator on the metric. Natural units are chosen such that $c = G = 1$. The Ricci tensor is a contraction of the Riemann tensor in the first and the third indices, i.e., $R_{ab} = R^{c}{}_{acb}$. The Riemann tensor can be computed from the metric g_{ab} and its connection $\Gamma^{a}{}_{bc} = \frac{1}{2} g^{ad} \left(-\partial_d g_{bc} + \partial_b g_{dc} + \partial_c g_{bd}\right)$ as

$$R^{a}{}_{bcd} = \partial_c \Gamma^{a}{}_{bd} - \partial_d \Gamma^{a}{}_{bc} + \Gamma^{e}{}_{bd} \Gamma^{a}{}_{ec} - \Gamma^{e}{}_{bc} \Gamma^{a}{}_{ed} \tag{2.2}$$

Written in terms of the metric components and their partial derivatives, Einstein's equations manifest their character as nonlinear partial differential equations of second order in the metric field, the quantity for which they are to be solved in a metric formulation.

GR being a relativistic theory, it's causal structure is defined by the light cone. The dynamical

quantity of GR is the gravitational field, which is encoded in the metric, and its perturbations propagate in the form of radiation. This gravitational radiation, also called gravitational waves, can be imagined as ripples of the spacetime curvature that travel at the speed of light.

In this thesis we worked with the Schwarzschild spacetime which is a vacuum solution to Einstein's equation. In this spacetime T vanishes, and the Einstein equations reduce to setting each component of the 4-dimensional Ricci tensor, ${}^{(4)}R_{ab}$ to zero. So wherever the source term appear in the equations in this thesis, they can be put to zero, unless explicitly indicated otherwise.

2.2 Gravitational Waves

In this thesis we worked with a spherically symmetric black hole solution of the Einstein's equations, namely the Schwarzchild solution. Since a spherically symmetric black hole does not radiate, we did not have to worry about wave extraction. But for the motivation to see why accurate and efficient numerical simulations of the sources generating gravitational waves are important we present a brief summary on gravitational waves.

Gravitational waves (GWs) were predicted by Einstein[4] in his study of the wave phenomena in linearized gravity. However, due to the physical and mathematical complexity of the theory, the coordinate dependent quantities involved in the calculations and the background independence of GR, the question of whether GWs were actual physical phenomena or simply coordinate effects was raised and it was not until the 1960s that the physical nature of GWs, interpreted as free gravitational degrees of freedom carrying positive energy[5] [6], was finally understood.

GWs are emitted by non-spherically accelerated massive objects and they have such a small amplitude that no direct observation has taken place so far. Thanks to the discovery of the binary pulsar PSR 1913+16 by Hulse and Taylor[1], their discovery gave an evidence for the existence of GWs. The pulsar forms a binary system with another neutron star, and the energy loss that causes the shrinking of the distance between both corresponds to the emitted GW radiation predicted by GR.

2.2.1 Radiation

From the theory of radiation field, a radiation must be able to carry energy to infinity. If the amplitude of the field a distance r from the source in the direction (θ, ϕ) is denoted by $A(r, \theta, \phi)$ then the flux through a spherical surface at that distance is

$$F(r, \theta, \phi) \propto A^2(r, \theta, \phi)$$

If we assume that the radiation is spherically symmetric, i.e., $A(r, \theta, \phi) = A(r)$ then the luminosity is

$$L(r) \propto A^2(r)\ 4\pi r^2$$

Expanding the static field of a source in moments, the slowest-decreasing moment (the monopole) decreases like $A(r) \propto 1/r^2$, implying that $L(r) \propto 1/r^2$ and hence no energy is carried to infinity. Two important conclusions can be made regardless of the nature of the radiation (electromagnetic or gravitational). First that the radiation requires time variation of the source and second that the amplitude must scale as 1/r far from the source.

For the case of gravitational radiation the monopole moment is $\int \rho(\mathbf{r}) d^3r$, which is simply the total mass-energy and that is a constant. Therefore, there cannot be monopolar gravitational radiation. The static dipole moment is $\int \rho(\mathbf{r})\mathbf{r} d^3r$ and this is just the center of mass-energy of the system. In the center of mass frame, therefore, this moment does not change, so there cannot be electric dipolar radiation in this frame (or any other, since the existence of radiation is frame-independent). The equivalent of the magnetic dipolar moment is $\int \rho(\mathbf{r})\mathbf{r} \times \mathbf{v}(\mathbf{r}) d^3r$. This is the total angular momentum of the system and so its conservation means that there is no magnetic dipolar gravitational radiation either. The next static moment is quadrupolar, $I_{ij} = \int \rho(\mathbf{r}) r_i r_j d^3r$ and this is not conserved, therefore there can be quadrupolar gravitational radiation.

This analysis gives some idea about the type of motion that can generate gravitational radiation. For example, a spherically symmetric variation is only monopolar, hence it does not produce radia-

tion. Next, a rotation that preserves axisymmetry (without contraction or expansion) does not generate gravitational radiation because the quadrupolar and higher moments are unaltered. For example, a neutron star can rotate arbitrarily rapidly without emitting gravitational radiation as long as it maintains axisymmetry.

2.2.2 Order of magnitude estimates

Here we would like to present an order of magnitude estimate as it shows why detecting gravitational waves is so challenging. This also motivates why the numerical simulations have to be very accurate and efficient as the numerical waveform will be important in the detection process.

When considering GWs, one often separates the spacetime into a component that is time-independent (the background spacetime) and a component that varies with time (the GWs). One also assumes that the measurements are far enough from the source such that the background spacetime is flat. The time-dependent metric produced by gravitational waves can then be written as

$$g_{ab} = \eta_{ab} + h_{ab} \tag{2.3}$$

where h_{ab} is very small such that one only considers its linear contribution to any equation. Therefore, the indices are raised or lowered using η^{ab} or η_{ab}, respectively . Using Eq.[2.3] one can construct the linearized version of the Einstein field equations. In the linearized version the field equations reduce to a wave equation. Two important results from the linearized version are (i) the waves are transverse, just like the electromagnetic waves, and (ii) there are two polarizations, different from the EM ones owing to the quadrupolar (spin-2) nature of gravitational waves.

One can do a *'back of the envelope calculation'* to compute the order of magnitude for the dimensionless amplitude h of a metric perturbation at a distance r from a source. As we saw, the lowest order radiation has to be quadrupolar, and hence depends on the quadrupole moment $I_{ij} = \int \rho(\mathbf{r}) r_i r_j d^3 r$, therefore $[I_{ij}] \equiv MR^2$, where M is some mass and R is a characteristic dimension. Since the ampli-

tude has to be proportional to $1/r$, we can write

$$h \sim MR^2/r$$

h should also be dimensionless but here it is $distance\ squared$[1](in geometric units where $G = c = 1$, mass, distance, and time all have the same effective units). Also, time derivatives have to be involved, since a static system can't emit anything. Two time derivatives will cancel out the present units and so we have

$$h \sim \frac{1}{r}\frac{\partial^2(MR^2)}{\partial t^2}$$

Restoring the above approximation back in the physical units by using appropriate factors of G and c[2] we get

$$h \sim \frac{G}{c^4}\frac{1}{r}\frac{\partial^2(MR^2)}{\partial t^2}$$

Now it is quite apparent that the prefactor is tiny, and so unless M and R are large, the system is rapidly changing, and r is small, the metric perturbation is minuscule. From this a rough estimate for a circular equal mass binary (scaled to a double neutron star) can be written as

$$h \approx 10^{-22}\left(\frac{M}{2.8M_\odot}\right)^{5/3}\left(\frac{0.01\ sec}{P}\right)^{2/3}\left(\frac{100\ Mpc}{r}\right)$$

2.3 The 3+1 (ADM) Formalism[7]

2.3.1 3+1 Foliation

In Einstein's treatment of gravity, time and space are kept on an equal footing. For solving the field equations numerically, it is important to transform the equations into a form in which they can be integrated forward in time. This is achieved by writing the field equations in the form of a Cauchy problem or an initial value problem. Once that is done, one has to find an appropriate initial data set. Then, to evolve the initial data set, one has to specify spatial boundary conditions and gauge

[1] or mass squared, or time squared

[2] If M is a mass, GM/c^2 has units of distance, and GM/c^3 has units of time

conditions. One way to achieve this is to follow 3+1 split that assumes a family of three-dimensional surfaces Σ_t that foliate spacetime with a continuous parameter t. At each point the ten equations of [2.1] can be projected onto the local hypersurface and onto the normal to that surface n^a . An observer who is falling along the normal will measure the proper interval α (i.e; $d\tau = \alpha dt$), called the lapse function between slices. Additionally he can have a spatial displacement vector β^a , called the shift vector, such that his time direction t^a is:

$$t^a = \alpha n^a + \beta^a \tag{2.4}$$

Where $n_a = -\alpha \nabla_a t$ and t^a is tangential to the time lines, the lines with constant spatial coordinates. In general $t_a \neq \nabla_a t$, because the previous relation yields $t_a = -\alpha^2 \nabla_a t + \beta_a$. Using the definitions of t^a and n_a we obtain that $t^a \nabla_a t = 1$, which means that t^a is a basis vector and $\nabla_a t$ is a basis covector.

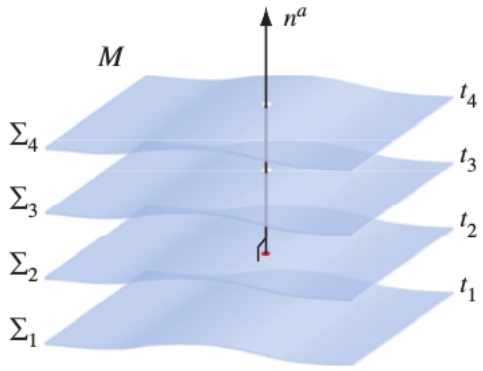

Figure 2.1: A foliation of the spacetime manifold $\mathcal{M}$. The hypersurfaces are level surfaces of the coordinate time t. The normal vector n^a is orthogonal to these t = constant spatial hypersurfaces.[7]

2.3.2 3+1 decomposition

Objects (tensors, vectors or one-forms) appearing in the equations are decomposed into spacelike and timelike parts by projecting them tangential to the spacelike surfaces (Σ_t) or perpendicular to them (along n^a), respectively. For projecting perpendicularly to Σ_t, a tensor is contracted with n^a . The projection tangential to Σ_t is performed using the projection operator

$$\gamma^a{}_b \equiv \delta^a{}_b + n^a n_b \tag{2.5}$$

to contract the quantities (this can be viewed as removing the timelike part). As an illustration of the 3+1 projection procedure, the decomposition of a tensor T^{ab} is given by

$$\begin{aligned} T^{ab} = \delta^a{}_c \delta^b{}_d T^{cd} &= (\gamma^a{}_c - n^a n_c)(\gamma^b{}_d - n^b n_d) T^{cd} \\ &= \underbrace{\gamma^a{}_c \gamma^b{}_d T^{cd}} - \underbrace{\gamma^a{}_c n^b n_d T^{cd} - \gamma^b{}_d n^a n_c T^{cd}} + \underbrace{n^a n_c n^b n_d T^{cd}} \\ & \quad \Sigma_{t\parallel} \qquad\qquad mixed\, terms \qquad\qquad \Sigma_{t\perp} \end{aligned} \tag{2.6}$$

Induced Metric

Projecting the *4-metric* onto the hypersurface Σ_t gives a spacelike projection of the metric (γ_{ab}) induced on Σ_t from the 4-metric g_{ab}. The 4-metric and the spacelike projected one are related as

$$\gamma_{ab} = \gamma^c{}_a \gamma^d{}_b g_{cd} \equiv g_{ab} + n_a n_b \tag{2.7}$$

where we used the relation $n^a \gamma_{ab} = 0$, which holds because γ_{ab} is spacelike.

The three dimensional space on the spacelike hypersurface Σ_t can be described using the three dimensional spatial part ofγ_{ab} , that will be denoted by γ_{ij}

$$dl^2 = \gamma_{ij} dx^i dx^j \tag{2.8}$$

Now to decompose g_{ab}, its components can be expressed in terms of α, β^i and γ_{ij}. For this, each of its components will have to be determined. They are given by $g_{\mu\nu} = g_{ab} e^a{}_\mu e^b{}_\nu$ as follows, where the relations $n^a n_a = -1$, $\beta^a n_a = 0$, $\beta^\mu = (0, \beta^i)$, $n_a \gamma^a{}_i = 0$ and $\beta_a \gamma^a{}_i = \beta_i$ have been used:

$$\begin{aligned} g_{00} &= g_{ab} e^a{}_0 e^b{}_0 = g_{ab} t^a t^b = t^a t_a = (\alpha n^a + \beta^a)(\alpha n_a + \beta_a) = -\alpha^2 + \beta^k \beta_k \\ g_{0j} &= g_{ab} e^a{}_0 e^b{}_j = t_b e^b{}_j = (\alpha n_b + \beta_b) \gamma^b{}_j = \beta_b \gamma^b{}_j = \beta_j \\ g_{i0} &= g_{ab} e^a{}_i e^b{}_0 = \cdots = \beta_i \\ g_{ij} &= g_{ab} e^a{}_i e^b{}_j = g_{ab} \gamma^a{}_i \gamma^b{}_j = \gamma_{ij} \end{aligned} \tag{2.9}$$

The metric g_{ab} and it's inverse g^{ab} can now be written in a matrix form as

$$g_{ab} = \begin{pmatrix} -\alpha^2 + \beta^k\beta_k & \beta_j \\ \beta_i & \gamma_{ij} \end{pmatrix} \quad and \quad g^{ab} = \frac{1}{\alpha^2}\begin{pmatrix} -1 & \beta^j \\ \beta^i & \alpha^2\gamma^{ij} - \beta^i\beta^j \end{pmatrix}$$

Now from Eq. [2.7] and using $n_a = (-\alpha, 0)$, and $n^a = \frac{1}{\alpha}(1, -\beta)$ we can write γ_{ab} and it's inverse γ^{ab} as

$$\gamma_{ab} = \begin{pmatrix} \beta^k\beta_k & \beta_j \\ \beta_i & \gamma_{ij} \end{pmatrix} \quad and \quad \gamma^{ab} = \begin{pmatrix} 0 & 0 \\ 0 & \gamma^{ij} \end{pmatrix}$$

The invariant distance between two infinitesimally separated events can now be written as

$$ds^2 = -\alpha^2 dt^2 + \gamma_{ij}(dx^i + \beta^i dt)(dx^j + \beta^j dt) \tag{2.10}$$

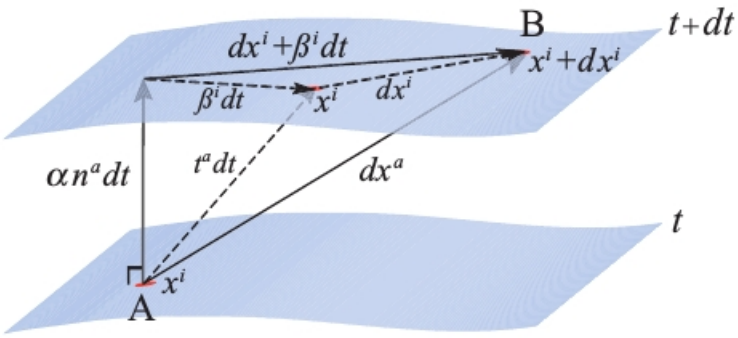

Figure 2.2: Pythagoras theorem in 3 + 1 dimensional spacetime. The normal vector αn^a and the time vector t^a connect points on two neighboring spatial slices. The shift vector β^i resides in the slice and measures their difference. The infinitesimal displacement vector dx^a connects two nearby, but otherwise arbitrary, points on neighboring slices (e.g., the point A at x^i on slice t and the point B at $x^i + dx^i$ on slice $t + dt$). The total displacement vector $dx^a = t^a dt + dx^i$, where dx^i is the spatial vector drawn in the figure, may be decomposed alternatively into two vectors that form the legs of a right-triangle, $dx^a = (\alpha n^a dt) + (dx^i + \beta^i dt)$, as shown. Using this decomposition to evaluate the invariant interval $ds^2 = dx^a dx_a$, yields the Pythagorean theorem, equation [2.5][7]

Extrinsic Curvature

One introduces the extrinsic curvature, K_{ab} , which describes the warping/deformation of the 3D slice in the 4D Lorentzian space in which it is embedded. This quantity is defined by projecting gradients of the normal vector, i.e., $\gamma^{c}{}_{a}\gamma^{d}{}_{b}\nabla_{c}n_{d}$. This projection is split into a symmetric part, known as the expansion tensor and an anitsymmetric part called the twist(rotation 2-form),

$$\begin{aligned}\theta_{ab} &= \gamma^{c}{}_{a}\gamma^{d}{}_{b}\nabla_{(c}n_{d)} \\ \omega_{ab} &= \gamma^{c}{}_{a}\gamma^{d}{}_{b}\nabla_{[c}n_{d]}\end{aligned} \tag{2.11}$$

The twist(ω_{ab}) is zero as a result of n^{a} being rotation free. The extrinsic curvature is now defined as the negative of the expansion

$$K_{ab} \equiv -\gamma^{c}{}_{a}\gamma^{d}{}_{b}\nabla_{(c}n_{d)} \tag{2.12}$$

Since n^{a} are normalized, they can only differ in the direction in which they are pointing, and the extrinsic curvature therefore shows how much this direction changes from point to point across a spatial hypersurface. Therefore, the extrinsic curvature measures the rate at which the hypersurface deforms as it is carried forward along a normal.

2.3.3 3+1 decomposition of the field equations

In order to express Einstein's equations in terms of the 3+1 variables, a spacelike equivalent to the covariant derivative ∇_{a} is formed by using the projection operator i.e., $D_{a} \equiv \gamma^{b}{}_{a}\nabla_{b}$. This acts on spatial tensors and follows the same property as the 4D covariant derivative i.e.,

$$D_{k}\gamma_{ij} = 0 = \gamma^{d}{}_{k}\gamma^{a}{}_{i}\gamma^{b}{}_{j}\nabla_{d}g_{ab}{}^{3} \tag{2.13}$$

[3] $\nabla_{d}g_{ab} = 0$ in order to define a connection that is metric compatible.

Projections of the Riemann tensor[4]

In order to cast the Einstein's equations [2.1] in 3+1 variables one has to first decompose the four-dimensional Riemann tensor ${}^{(4)}R^{a}{}_{bcd}$. This requires three independent projections:

- Projecting all the indices onto the spacelike hypersurface Σ_t : *Gauss's* equations

$$\gamma^{e}{}_{a}\gamma^{f}{}_{b}\gamma^{g}{}_{c}\gamma^{h}{}_{d}{}^{(4)}R_{efgh} = R_{abcd} + K_{ac}K_{bd} - K_{ad}K_{bc} \tag{2.14}$$

- Projecting onto Σ_t the Riemann tensor contracted once with the normal vector : *Codazzi's* equations

$$\gamma^{e}{}_{a}\gamma^{f}{}_{b}\gamma^{g}{}_{c}n^{d(4)}R_{efgd} = D_bK_{ac} - D_aK_{bc} \tag{2.15}$$

- Projecting onto Σ_t the Riemann tensor contracted twice with the normal vector : *Ricci's* equations

$$\gamma^{e}{}_{a}\gamma^{f}{}_{c}n^{b}n^{d(4)}R_{ebfd} = \mathcal{L}_{\mathbf{n}}K_{ac} + \frac{1}{\alpha}D_aD_c\alpha + K^{d}{}_{c}K_{ad} \tag{2.16}$$

The 3+1 equations

Now one just needs to take the equations of Gauss[2.14], Codazzi[2.15] and Ricci[2.16] and eliminate the 4-dimensional Riemann tensor using Einstein's equations[2.1]. The following results will be used in the decomposition of the Einstein equations:

$$\begin{aligned}\gamma^{ac}\gamma^{bd(4)}R_{abcd} &= {}^{(4)}R + 2n^{a}n^{b(4)}R_{ab} = 2n^{a}n^{b(4)}G_{ab}\\ \gamma^{ab}n^{c(4)}R_{bc} &= \gamma^{ab}n^{c(4)}G_{bc}\end{aligned} \tag{2.17}$$

Contracting the Gauss equation[2.14] twice using γ^{ab} we get

$$\gamma^{ac}\gamma^{bd(4)}R_{abcd} = R + K^2 - K_{ab}K^{ab} \tag{2.18}$$

[4]For complete derivation refer [7]

where $K \equiv K^a{}_a$ is the trace of the extrinsic curvature. Now using Eqs.[2.1], [2.17] and [2.18], and defining the energy density ρ to be the total energy density($\rho \equiv n_a n_b T^{ab}$) as measured by a normal observer n^a we get

$$R + K^2 - K_{ab}K^{ab} = 16\pi\rho \tag{2.19}$$

From the Codazzi Eq.[2.15] and using Eq[2.17] we get:

$$\gamma^{ab} n^{c\,(4)}R_{bc} = \gamma^{ab} n^{c\,(4)}G_{bc} = D^a K - D_b K^{ab} \tag{2.20}$$

Using Eq[2.1] and writing $S^a \equiv -\gamma^{ab} n^c T_{bc}$ for the momentum density measured along the normal direction we get

$$D_b K^{ab} - D^a K = 8\pi S^a \tag{2.21}$$

Contracting only once the Gauss equation[2.14] yields the following relation:

$$\gamma^d{}_a \gamma^f{}_b \left({}^{(4)}R_{df} + n^c n^{e\,(4)}R_{cdef}\right) = R_{ab} + K K_{ab} - K_{ac}K^c{}_b \tag{2.22}$$

Now using Ricci Eq[2.16] for substituting the second term in the above equation and using projection of the Einstein equations written in terms of the Ricci tensor [5] to substitute for the first term, we get:

$$\mathcal{L}_{\mathbf{t}} K_{ab} = -D_a D_b \alpha + \alpha \left(R_{ab} - 2K_{ac}K^c{}_b + K K_{ab}\right) - 8\pi\alpha \left(S_{ab} - \frac{1}{2}\gamma_{ab}(S - \rho)\right) + \mathcal{L}_{\bar{\beta}} K_{ab} \tag{2.23}$$

where we have used the relations $\mathcal{L}_{\mathbf{t}} \equiv \mathcal{L}_{\alpha\mathbf{n}+\bar{\beta}} \equiv \alpha\mathcal{L}_{\mathbf{n}} + \mathcal{L}_{\bar{\beta}}$, $S_{ab} \equiv \gamma^c{}_a \gamma^d{}_b T_{cd}$ and $S \equiv S^a{}_a$. Above is the evolution equation for the extrinsic curvature. The extrinsic curvature can also be defined as the *Lie derivative* along the normal n^a of the spatial metric γ_{ab}

$$K_{ab} = -\frac{1}{2}\mathcal{L}_{\mathbf{n}}\gamma_{ab} = -\frac{1}{2\alpha}\left(\mathcal{L}_{\mathbf{t}}\gamma_{ab} - \mathcal{L}_{\bar{\beta}}\gamma_{ab}\right) \tag{2.24}$$

[5] $\gamma^c{}_a \gamma^d{}_b {}^{(4)}R_{cd} = \gamma^c{}_a \gamma^d{}_b \left(8\pi {}^{(4)}T_{cd} - \frac{1}{2} g_{cd} g^{ef\,(4)}T_{ef}\right)$

This gives the evolution equation for the spatial metric. Eq.[2.19] is the *Hamiltonian constraint* and Eq.[2.21] is the *momentum constraint*. The constraint equations are to be satisfied on each of the spatial hypersurfaces. Eq.[2.23] and Eq.[2.24] are the evolution equations. Eqs.[2.19], [2.21], [2.23] and [2.24] are collectively called the ADM [6] equations.

Analytically, the evolution equations are guaranteed to preserve the constraint equations. Numerically, however, they do not due to numerical errors. Therefore, it is important to monitor the constraint equations during the evolution, in order to gauge the size of numerical errors.

2.4 The BSSN Formalism

The BSSN [7] system is based on the *York-Lichnerowicz Conformal Decomposition* and rewrites the above ADM equations [2.19], [2.21], [2.23] and [2.24] to deal with the numerical instabilities. First the spatial metric γ_{ij} is decomposed into a conformally related metric $\bar{\gamma}_{ij}$ with determinant $\bar{\gamma} = 1$[8] (assuming Cartesian coordinates) and a conformal factor ψ followed by the split of the extrinsic curvature into a trace-free A_{ij} and a trace part K. The traceless part is then conformally transformed as we do for the metric,

$$\begin{aligned} \gamma_{ij} &= \psi^4 \, \bar{\gamma}_{ij} \, , \\ K_{ij} &= \psi^4 \tilde{A}_{ij} + \frac{1}{3}\gamma_{ij} K \end{aligned} \tag{2.25}$$

The Hamiltonian constraint [2.19] becomes

$$\bar{\gamma}^{ij}\bar{D}_i\bar{D}_j\psi - \frac{\psi}{8}\bar{R} + \frac{\psi^5}{8}\tilde{A}_{ij}\tilde{A}^{ij} - \frac{\psi^5}{12}K^2 + 2\pi\psi^5\rho = 0 \tag{2.26}$$

while the momentum constraint [2.21] becomes

$$\bar{D}_j(\psi^6\tilde{A}^{ij}) - \frac{2}{3}\psi^6\bar{D}^i K - 8\pi\psi^6 S^i = 0 \tag{2.27}$$

[6] Arnowitt-Deser-Misner

[7] Baumgarte-Shapiro-Shibata-Nakamura

[8] Appropriate in the case of Cartesian coordinates, but it is incompatible with coordinates adapted to spherical symmetry. This constraint is relaxed in the Generalized BSSN (GBSSN) formalism

The evolution equation [2.24] for γ_{ij} splits into two equations,

$$\begin{aligned}\partial_t ln\psi &= -\frac{1}{6}\alpha K + \beta^i \partial_i ln\psi + \frac{1}{6}\partial_i \beta^i \ , \\ \partial_t \bar{\gamma}_{ij} &= -2\alpha \tilde{A}_{ij} + \beta^k \partial_k \bar{\gamma}_{ij} + \bar{\gamma}_{ik}\partial_j \beta^k + \bar{\gamma}_{kj}\partial_i \beta^k - \frac{2}{3}\bar{\gamma}_{ij}\partial_k \beta^k\end{aligned} \tag{2.28}$$

while the evolution equation [2.23] for K_{ij} splits into the two equations

$$\begin{aligned}\partial_t K &= -\gamma^{ij} D_j D_i \alpha + \alpha(\tilde{A}_{ij}\tilde{A}^{ij} + \frac{1}{3}K^2) + \beta^i \partial_i K \ , \\ \partial_t \tilde{A}_{ij} &= \psi^{-4}(-(D_i D_j \alpha)^{TF} + \alpha R_{ij}^{TF}) + \alpha(K\tilde{A}_{ij} - 2\tilde{A}_{il}\tilde{A}^l{}_j) \\ &\quad + \beta^k \partial_k \tilde{A}_{ij} + \tilde{A}_{ik}\partial_j \beta^k + \tilde{A}_{kj}\partial_i \beta^k - \frac{2}{3}\tilde{A}_{ij}\partial_k \beta^k\end{aligned} \tag{2.29}$$

TF denotes the trace-free part of a tensor, e.g., $R_{ij}^{TF} = R_{ij} - \gamma_{ij}R/3$. The Ricci tensor is also split into $R_{ij} = \bar{R}_{ij} + R_{ij}^{\psi}$, where R_{ij}^{ψ} is given by

$$\begin{aligned}R_{ij}^{\psi} &= \bar{R}_{ij} - 2\left(\bar{D}_i \bar{D}_j ln\psi + \bar{\gamma}_{ij}\bar{\gamma}^{lm}\bar{D}_l \bar{D}_m ln\psi\right) \\ &\quad + 4\left((\bar{D}_i ln\psi)(\bar{D}_j ln\psi) - \bar{\gamma}_{ij}\bar{\gamma}^{lm}(\bar{D}_l ln\psi)(\bar{D}_m ln\psi)\right)\end{aligned} \tag{2.30}$$

Next $\bar{R}_{ij}$ is expressed in terms of the conformal connection functions $\bar{\Gamma}^i \equiv \bar{\gamma}^{jk}\bar{\Gamma}^i_{jk} = -\partial_j \bar{\gamma}^{ij}$ that gives

$$\bar{R}_{ij} = -\frac{1}{2}\bar{\gamma}^{lm}\partial_m \partial_l \bar{\gamma}_{ij} + \bar{\gamma}_{k(i}\partial_{j)}\bar{\Gamma}^k + \bar{\Gamma}^k \bar{\Gamma}_{(ij)k} + \bar{\gamma}^{lm}\left(2\bar{\Gamma}^k_{l(i}\bar{\Gamma}_{j)km} + \bar{\Gamma}^k_{im}\bar{\Gamma}_{klj}\right) \tag{2.31}$$

The $\bar{\Gamma}^i$ are now treated as independent functions that satisfy their own evolution equations,

$$\begin{aligned}\partial_t \bar{\Gamma}^i &= -2\tilde{A}^{ij}\partial_j \alpha + 2\alpha\left(\bar{\Gamma}^i_{jk}\tilde{A}^{kj} - \frac{2}{3}\bar{\gamma}^{ij}\partial_j K + 6\tilde{A}^{ij}\partial_j \phi\right) \quad + \beta^j \partial_j \bar{\Gamma}^i \\ &\quad - \bar{\Gamma}^j \partial_j \beta^i + \frac{2}{3}\bar{\Gamma}^i \partial_j \beta^j + \frac{1}{3}\bar{\gamma}^{li}\partial_l \partial_j \beta^j + \bar{\gamma}^{lj}\partial_j \partial_l \beta^i\end{aligned} \tag{2.32}$$

For a complete derivation refer[7].

2.5 Solving the Initial Data Problem

In order to obtain the spacetime that satisfies the Einstein's equations one has to specify the gravitational fields (γ_{ij}, K_{ij}) on some initial spatial slice Σ that are compatible with the constraint equations. Once these fields are specified, they can be used as initial values for a dynamical evolution obtained by integrating the evolution equations.

There are different approaches for getting the initial data and more details can be found here[7] [8]. One obvious way to obtain initial data that is compatible with constraints is to directly use analytical solutions to the Einstein equations. In the work presented here we used the *'trumpet'* data[9] which was obtained by considering a known spacetime, namely, the Schwarzschild spacetime in (quasi or spatially) isotropic coordinates

$$ds^2 = -\left(\frac{1-\frac{M}{2r}}{1+\frac{M}{2r}}\right)^2 dT^2 + \left(1+\frac{M}{2r}\right)^4 \left[dr^2 + r^2(d\theta^2 + sin^2\theta d\phi^2)\right] \tag{2.33}$$

2.5.1 Schwarzschild Solution

Schwarzschild solution depicts a static spacetime containing a single black hole, the union of two causally disconnected and asymptotically flat geometries[21] [22]. The Schwarzschild metric in the standard Schwarzschild coordinates is given by the line element

$$ds^2 = -\left(1-\frac{2M}{R}\right) dT^2 + \left(1-\frac{2M}{R}\right)^{-1} \left(dR^2 + R^2 d\Omega^2\right) \tag{2.34}$$

where M is the mass of the Schwarzschild black hole as measured at spacelike infinity.There are some interesting and surprising features of the geometry described by this metric:

- R = 2M is known as event horizon. It can be thought of as the boundary that separates the inner and outer part of the black hole.
- As R approaches 2M, the coefficient of timelike part approaches zero, and the coefficient of spacelike part approaches infinity.

- R = 2M is a coordinate singularity that can be removed by coordinate transformation (like the transformation to isotropic coordinates)
- R = 0 is a physical singularity and cannot be removed by any transformation. Moreover, curvature scalars become infinite as $R \to 0$.

The isotropic coordinate is related to the standard Schwarzschild coordinate by

$$r = \psi^{-2} R \tag{2.35}$$
$$Where\ \psi = 1 + \frac{M}{2r}$$

The isotropic r does not reach the physical singularity at $R = 0$. For large r we see that $R \to \infty$, but for small r we see that once again $R \to \infty$. There is a minimum of $R = 2M$ at $r = M/2$. We now have two copies of the space outside the event horizon, $R > 2M$, and the two spaces are connected by a wormhole with a throat at $R = 2M$.

We would like to clarify here that the numerical evolution of an analytically known spacetime does not give any new physical insight. But it serves as an important way to test numerical codes. Importantly, analytically known solutions often form the basis to construct generalized classes of initial data for which the time evolution is not known a priori, without numerical study. In this work we did not work on generating these data and so one can refer them here[9].

One can in principle use the Schwarzschild metric in the isotropic coordinates and identify 'initial' variables (ψ,γ_{ij}, K_{ij}, α, etc.) and use them as the initial data, also known as the *wormhole* initial data, Figure[2.3(a)]. But it is difficult to evolve them numerically in a standard 3D black-hole evolution code as most codes are not stable when the lapse, which here is $\left(\frac{1-\frac{M}{2r}}{1+\frac{M}{2r}}\right)$, is negative, this happens here for $r < M/2$[9]. This motivates the use of *'trumpet'* data.

2.5.2 Wormholes to 'trumpets'

When the wormhole initial data is evolved with the "1+log" slicing condition for the lapse and a "$\bar{\Gamma}$-driver" gauge condition for the shift[9], the solution passes through a short phase of "dynamical"

evolution, but then settles down into a new equilibrium solution. An embedding diagram of this new equilibrium solution is shown in Figure[2.3(b)] and suggests the name "trumpet" data. The solution terminates at a non-zero areal radius, and therefore does not encounter the spacetime singularity at the center of the black hole. The singularity at the isotropic radius $r = 0$ is a coordinate singularity only. This new equilibrium is a stationary slice of the "1 + log" slicing condition relative to the standard timelike Killing vector of the Schwarzschild solution.

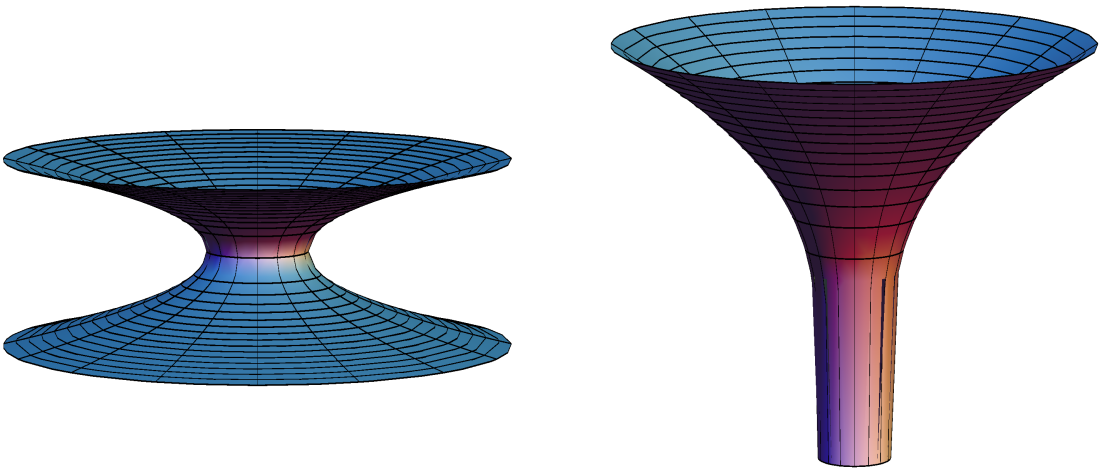

(a) Wormhole (b) 'Trumpet'

Figure 2.3: [a]Embedding diagram of a two-dimensional slice (T = const., $\theta = \pi/2$) of the extended Schwarzschild solution. The distance to the rotation axis is R. A wormhole with a throat at R = 2M connects two asymptotically flat ends. [b] Embedding diagram of a two-dimensional slice (t = const., $\theta = \pi/2$) of the maximal solution. The distance to the rotation axis is R. In contrast to Figure [a] there is only one asymptotically flat end. The other end is an infinitely long cylinder with radius $R_0 = 3M/2$.[9]

2.6 Gauge Conditions: the lapse and shift

The Einstein equations do not specify evolution equations for the lapse function α or the shift vector β^i. These are the gauge quantities related to the gauge freedom in Einstein's theory and can be chosen at will, at least theoretically. Though the physical properties of a spacetime remain unchanged under gauge transformations, the performance of numerical evolution schemes depends sensitively on the gauge choice. For example, it is well-known that the evolution of the Schwarzschild spacetime using geodesic slicing $\alpha = 1$ and vanishing shift $\beta^i = 0$ reach a hypersurface containing the black hole

singularity after a coordinate time interval $t = \pi M$ [10]. In such scenarios the singular functions output non-assigned numbers which rapidly swamp the entire computational domain and crash the evolution even before it is complete.

One can avoid such problems by using a lapse function that slows the evolution in proper time near the region of singular points in the spacetime[11]. Such slicing conditions are called *singularity avoiding* and have been studied systematically in the form of the Bona-Massó family of slicing conditions[12]. A problem that can arise from the use of singularity avoiding slicing is that the proper time can progress at different rates in different regions of the numerical domain resulting in a phenomenon referred to as "grid stretching" or "slice stretching". This can be nullified with suitable non-zero choices for the shift vector β^i.

We used the Gamma driver shift condition and a variant of the 1+log slicing condition. Therefore, we outline some of the key points about them in this thesis.

2.6.1 Gamma driver shift condition

The variant of the $\bar{\Gamma}$-driver condition[9] that was used is given by

$$\begin{aligned} \partial_t \beta^i &= \frac{3}{4} B^i \,, \\ \partial_t B^i &= \partial_t \bar{\Gamma}^i - \eta B^i \end{aligned} \tag{2.36}$$

where $\bar{\Gamma}^i \equiv -\partial_j \bar{\gamma}^{ij}$ are the conformal connection functions built from the conformal metric $\bar{\gamma}^{ij}$. The conformal metric has unit determinant, $\bar{\gamma} = 1$. B^i is an auxiliary quantity used to convert the second-order $\bar{\Gamma}$-driver shift condition into a pair of first-order equations, and η is a user prescribed term used to control dissipation in the simulation. This shift condition is important in the moving-puncture simulations. In binary black hole simulations such a shift generates motion of the punctures around the grid on trajectories that mimic the motion that would be seen from infinity. Since we were working with the Schwarzschild solution, there was no motion of the the puncture.

2.6.2 '1+log' slicing condition

For foliating the spacetime we used the '1+log' slicing condition which is often employed in dynamical moving puncture simulations and is given by,

$$(\partial_t - \beta^i \partial_i)\alpha = -2\alpha K \tag{2.37}$$

this slicing is "covariant" in the sense that it does not depend on the choice of the shift - for a given slice, and a given initial lapse, the resulting slicing of the spacetime is unique.

2.7 Discretization of the equations

Once one has a snapshot of the physical system at $t = 0$, the evolution equations, which in this work are the BSSN equations [2.28]-[2.32], will then evolve the system forward in time. These evolution equations are a set of nonlinear partial differential equations which relate a number of grid variables and their time and spatial derivatives. For their numerical implementation one needs to translate these differential equations into expressions relating arrays of numbers.

The two common methods to discretize these equations are finite differencing and spectral methods. Spectral methods are particularly efficient and accurate for numerical modelling when the functions do not develop discontinuities. The singularities in the black hole spacetimes can be excised as originally suggested by Unruh[13] . According to Penrose's cosmic censorship conjecture, "there are no naked singularities" i.e., a spacetime singularity should be hidden inside an event horizon and the spacetime region outside the event horizon is causally disconnected from the dynamics inside. In particular, excising a finite region around the singularity but within the horizon should leave the exterior spacetime unaffected.

In this work we used the BAM code [9]. It is a fully general relativistic finite difference code that is capable of simulating multiple black holes before and through merger. It uses a Cartesian grid with adaptive mesh refinement. Evolutions are performed using the BSSN system with the gamma-driver

[9]Developed by Bernd Brügmann, *Universität Jena*; BAM : Bi-functional Adaptive Mesh

shift and 1 + log-slicing gauge conditions.

2.7.1 Convergence test for the BAM code

The validity of the code was examined by a series of convergence tests. The accurate implementation of the numerical method is thus tested. The underlying idea relies on the fact that the overall error of a discretization should behave in a foreseeable manner when the resolution is increased. The basic assumption for finite difference approximations is the possibility to expand the solution in a Taylor series around a point. Assume a function f is computed with a finite differencing stencil of order n. Then for a fixed resolution h and multiple of it the solutions can be written as

$$\begin{aligned} f_h &= f_{exact} + C\ h^n + O(h^{n+1}), \\ f_{2h} &= f_{exact} + C\ (2h)^n + O(h^{n+1}), \\ f_{4h} &= f_{exact} + C\ (4h)^n + O(h^{n+1}) \end{aligned} \tag{2.38}$$

where the constant C does not depend on h. Taking differences and neglecting higher order error terms one gets

$$f_{4h} - f_{2h} = \frac{4^n - 2^n}{2^n - 1}(f_{2h} - f_h) = 2^n(f_{2h} - f_h) \tag{2.39}$$

The prefactor 2^n is often called the convergence factor, which can easily be generalized to the case where the resolutions are not simple multiple of each other.

We used a version of the code that was written with a fourth-order stencil and therefore we expected a fourth-order convergence.

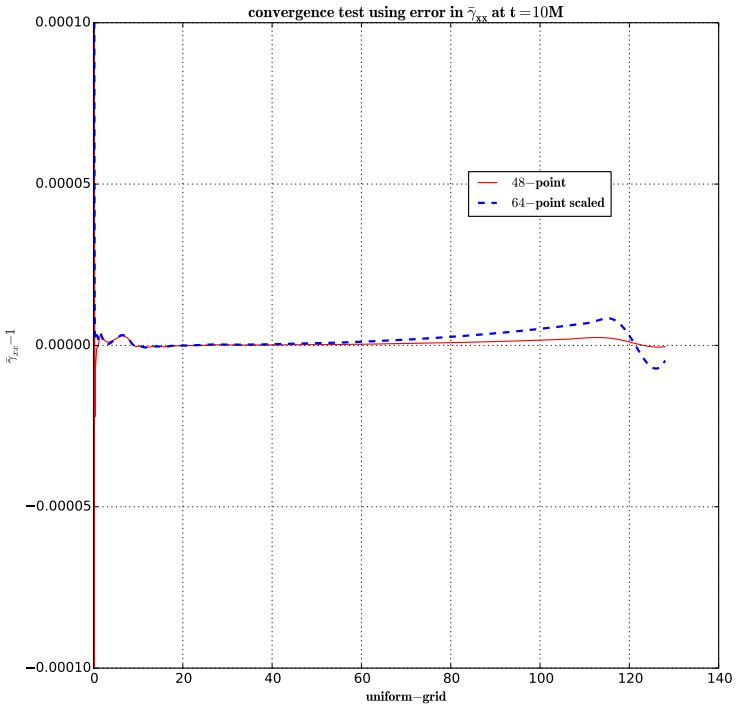

(a) full range of x

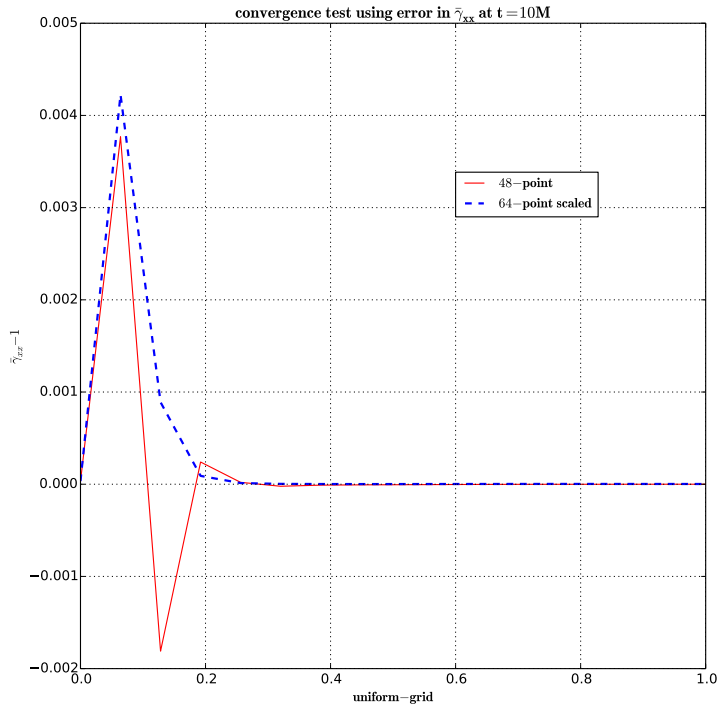

(b) near the puncture

Figure 2.4: The error in $\bar{\gamma}_{xx}$ (i.e.,$\bar{\gamma}_{xx} - 1$) after 10M of evolution of the time-independent trumpet puncture data. The errors for simulations at two resolutions (48 and 64-point) are scaled assuming fourth-order convergence, and we indeed see that the errors converge to zero at fourth-order.

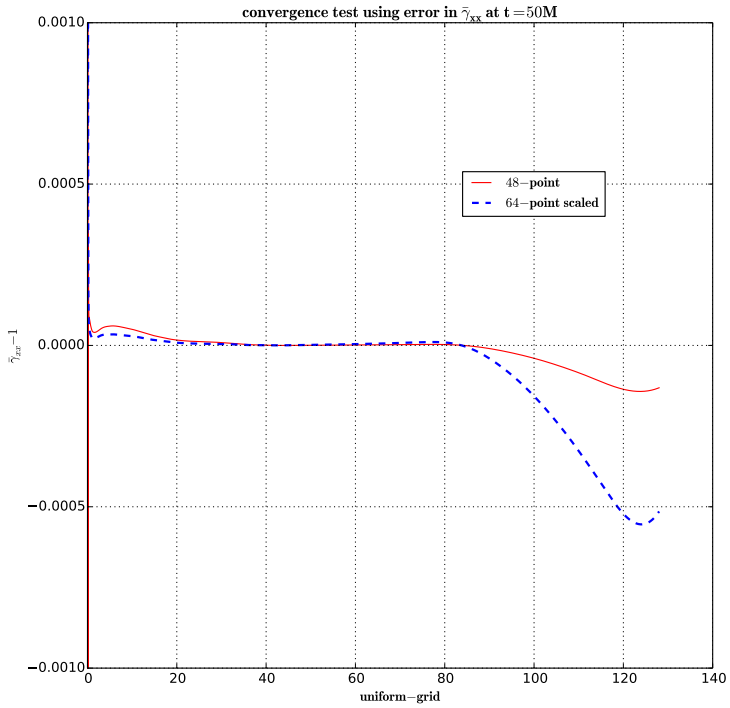

(a) full range of x

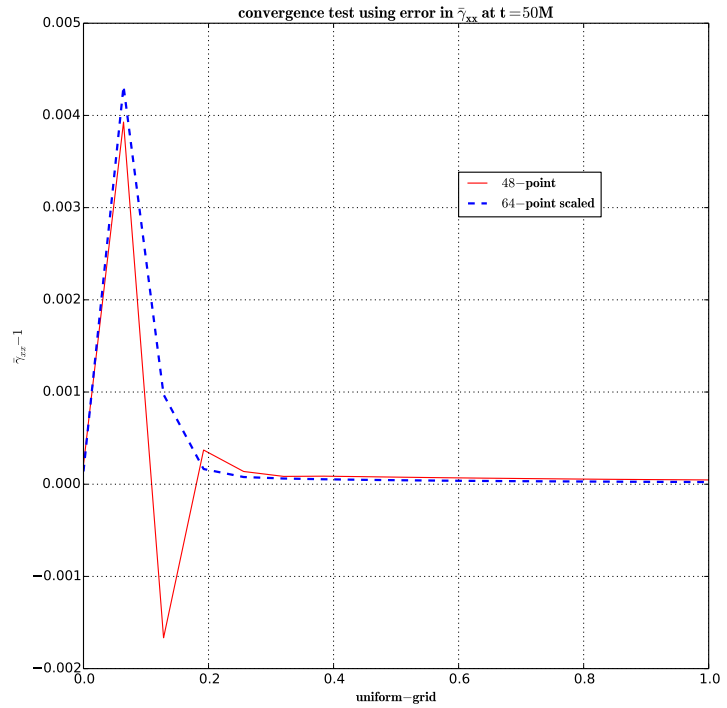

(b) near the puncture

The errors are scaled consistent with fourth-order convergence, and we indeed see fourth-order

convergence up to around x = 80M . Since the outer boundary is at x = 128M , by t = 50M lower-order errors from the outer boundary will have propagated to around x = 80M at speed of light, and so we do not expect to see fourth-order convergence beyond this point. After 100M of evolution the boundary errors would have propagated close to the puncture.

These plots confirm that the 'trumpet' data that we used are indeed time independent, within small numerical errors that converge to zero at the expected rate, i.e., fourth-order convergence. Since the analytic value of $\bar{\gamma}_{xx}$ is unity, we can calculate the percentage error from the plots: we see that at t = 10M the largest error in $\bar{\gamma}_{ij}$ is 0.001 % and at t=50M this 0.05 %, for the 64-point resolution simulation. One can also infer that the time-independent 'trumpet' data provide an excellent testing ground for the accuracy of a numerical code[9]. The BAM code uses the moving-puncture approach which is currently the most popular method for simulating black-hole binaries. There is no analytic black-hole solution that can be used to test such codes, except for the 1+log and stationary maximal trumpet solutions that we used in this work. These analytic solutions are important not only for testing a new code, but also in analysing and reducing the sources of error in existing codes.

Chapter 3

Apparent Horizons

3.1 Trapped Surfaces

One diagnostic tool that is used during the evolution of the system is the *apparent horizon*. It can be thought of as a surface of a black hole at one instant of time. It has several applications in numerical relativity, in particular to make estimates of the black-hole mass and angular momentum. In this work we will use the apparent horizon as one measure of the size of the black hole on the numerical grid. This is important when one wants to gauge the amount of resolution required to resolve the black hole, because using arbitrarily fine resolution may make the computation slow and very expensive.

The *event horizon* on the contrary is a concept that depends on the entire spacetime. It is defined as the boundary between points in the spacetime from which null geodesics can escape to infinity and points from which they cannot. In the context of numerical simulations, this implies that an event horizon can only be computed if information about the entire spacetime is stored which is not feasible even by modern standards [1]. Understanding the dynamics of the apparent horizon based on the modification to the $\bar{\Gamma}$-driver shift condition is the main focus in this thesis.

Definitions that are valid within only one time-slice are here called *quasi-local*. The quasi-local description of a region from which even light can not escape is based on trapped surfaces that in turn are defined by their expansions (divergences).

[1] Though event horizon finders have been developed in [14] [15]

Consider a null geodesic congruence. In an open subset $\mathcal{O}$ of a manifold a congruence is a family of curves such that through each point in $\mathcal{O}$ there passes precisely one curve in this family. The tangents k^a to these curves describe a vector field on $\mathcal{O}$. The tensor field $B_{ab} = \nabla_a k_b$ describes how neighbouring tangents behave. The expansion measures the average 'spread' of infinitesimally nearby geodesics. It is defined as

$$\Theta = m^{ab}\nabla_a k_b \tag{3.1}$$

where m_{ab} is the 2-dimensional metric induced by γ_{ab} on the geodesic congruence and is given by

$$m_{ab} = \gamma_{ab} - s_a s_b = g_{ab} + n_a n_b - s_a s_b \tag{3.2}$$

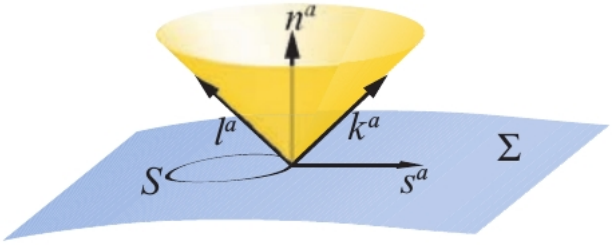

Figure 3.1: A smooth, 2D, hypersurface S is embedded in Σ . The unit, outward-pointing normal to S lying in Σ is s^a , and the normal to Σ is n^a . The outgoing and ingoing null tangent vectors k^a and l^a are constructed as linear combinations of n^a and s^a [7].

An *outer trapped surface* is defined as a 2D surface S embedded in Σ on which the expansion Θ of the outgoing null geodesics orthogonal to S is negative everywhere. A *trapped region* is defined as the region of Σ that contains outer trapped surfaces. The *apparent horizon* is the outer boundary of any connected trapped region. This makes the apparent horizon a *marginally outer trapped surface* (MOTS) on which the expansion of outgoing null geodesics vanishes, i.e.,

$$\Theta = \nabla_a k^a = 0 \tag{3.3}$$

These definitions are still in the 4D manifold and can be broken down to the objects of the 3+1 split, that are the metric γ_{ij} and the extrinsic curvature K_{ij}. The condition $\Theta = 0$ for every outward unit

normal s^i on a marginally outer trapped surface is

$$\begin{aligned}\sqrt{2}\,\Theta &= m^{ij}\left(D_i s_j - K_{ij}\right) = 0 \\ \sqrt{2}\,\Theta &= D_i s^i - K + K_{ij}s^i s^j = 0\end{aligned} \tag{3.4}$$

In the search for apparent horizons it is useful to characterize the horizon as a level surface of a scalar function, i.e.,

$$\tau(x^i) = 0 \tag{3.5}$$

and therefore, the unit normal s^i can be written as $s^i = \lambda D^i\tau$, or $s_i = \lambda D_i\tau = \lambda\partial_i\tau$, where λ is a normalization factor given by $\lambda = \left(\gamma^{ij}D_i\tau D_j\tau\right)^{-1/2}$. Using the new form of s^i in Eq.[3.4] and using the result $D^i\tau = 0$ we get,

$$m^{ij}\left(D_i s_j - K_{ij}\right) = m^{ij}\left(\lambda D_i D_j\tau - K_{ij}\right) = m^{ij}\left(\lambda\partial_i\partial_j\tau - s_k\Gamma^k{}_{ij} - K_{ij}\right) = 0 \tag{3.6}$$

A useful form of the level function τ in spherical polar coordinates is

$$\tau(x^i) = r - h(\theta,\phi) = 0 \tag{3.7}$$

so that the given function $h(\theta,\phi)$ measures the coordinate distance from the center (corresponding to r = 0) of the black hole to the $\tau(x^i) = 0$ surface in the (θ,ϕ) direction. Now the apparent horizon condition[3.6] reduces to

$$\sqrt{2}\,\Theta = m^{ij}\left(\lambda\partial_i\partial_j h - s_k\Gamma^k{}_{ij} - K_{ij}\right) = 0 \tag{3.8}$$

The apparent horizon condition[3.7] is a second-order partial differential equation for the function h that measures the horizon's coordinate distance from the origin (centre of the black hole). The first term of the equation, $m^{ij}\partial_i\partial_j h$, involves a Laplacian with respect to the 2D metric m^{ij} on the surface S. Finding solutions to these elliptic equations, and hence locating apparent horizons, is in general a

difficult task because the normal vector s^i also contains derivatives of h.

Apparent horizons are used during a simulation as an approximation of the location of the event horizon, and is thus especially useful for simulations that excise the black hole region including the singularity or as in our case for gauging the size of the black hole on the numerical grid. The location of the apparent and the event horizon coincides for stationary spacetimes (and suitable spatial hypersurfaces) but because of the slicing dependence the apparent horizon is not a good indicator for *cosmic censorship*[16].

3.2 Apparent Horizon Finder

Over the years several finders for apparent horizons were studied. They vary both in the description of the surface and in the choice of the actual solving procedure of the differential equation. Detailed survey can be found in Thornburg's Living Review[17].

The elliptic partial differential equation[3.8] can be tackled by a variety of methods. The most prominent distinction is that of a local and a global algorithm. Most apparent horizon finders are local, meaning they need a good initial guess to find the horizon. On the other hand these methods are often faster. An algorithm is called 'global' if it can also handle initial guesses not close to the solution. *Flow algorithms* are known to have this feature. BAM uses an apparent horizon finder (AHF) module that is based on the flow algorithm.

Flow methods stand out for their robustness against bad initial guesses. They define a gradual change of the initial surface proportional to the local expansion. Near to the apparent horizon with expansion $\Theta = 0$ the speed will also tend to zero. Special choices of the flow functions must be applied. One major improvement was introduced by Gundlach's[18] 'fast-flow' algorithm. He iterates each mode of the surface with different speed, thus high frequency modes do not slow down down the evolution. His method is based on the spectral code that Nakamura et. al. developed in 1984[19].

3.2.1 The BAM Apparent Horizon Finder

The BAM apparent horizon finder (AHF) uses the fast flow method. AHF was coded by José Antonio González based on a previous routine that was implemented by Miguel Alcubierre in Fortran. The basic version was thoroughly tested with several orders of their spectral expansion and various numbers of points on the grid in [20].

Several missing features were established that were needed for this study. First not only the outermost trapped surface can be found but also the inner ones. Secondly the location for each surface is saved and used as the initial guess of the next search. Additionally the time periods throughout the evolution at which a specific surface is searched for can be given as input. Specifying the search window prevents the apparent horizon finder from costly searches for the common horizon long before merger; the disadvantage being that the time of merger should be roughly known beforehand.

The accuracy of the horizon finder can be selected in several ways. One aspect is the maximal degree *LMAX* of the spherical harmonics that represent the surface. Its value was mostly kept at *LMAX*$= 10$, but could have been set to a lower value as we were working with the Schwarzschild black hole. Being spherically symmetric, only the monopole term (l=0) is non-zero. During the run the expansion is calculated at specific positions given by a regular angular grid, the grid size we used was $n\theta \times n\phi = 100 \times 200$. This choice comes from the logic that the spectral expansion of order *LMAX* has angular distributions up to $\cos(LMAX\pi)$. Four points per cycle are needed at least, a better resolution can use eight or ten points. Thus $10 \times$ *LMAX* points in ϕ-direction should be an adequate number.

One other parameter is the stopping criteria of the flow. For each surface the mass is calculated from its area as $mass = \sqrt{area/(16\,\pi)}$. When the change of the mass between steps drops below a certain tolerance, the flow has converged. This tolerance was kept at $\sim 10^{-5}$.

3.3 Modified BAM Code

For this thesis we modified the BAM code such that a new component is added to the existing $\bar{\Gamma}$-driver shift that allows us to move the horizon to a desired location. Since the $\bar{\Gamma}$-driver shift is a gauge condition i.e., we are free to choose the shift (β^i) as we please, the physics does not change. But when one wants to implement the gauge freedom for numerical simulations it has been seen that some shift conditions handle numerical errors more robustly than others. The $\bar{\Gamma}$-driver shift is one class of shift conditions that has been tested and is the workhorse for the 'moving-puncture' simulations used in this thesis.

3.3.1 Horizon adjusting shift

There were two important aspects to consider while modifying the $\bar{\Gamma}$-driver condition:

- Firstly, it should maintain the global properties of the $\bar{\Gamma}$-driver condition, and
- secondly, allow us to move the apparent horizon to a desired, given location.

as such we write the shift as the sum of two components,

$$\beta^i = \beta^i_{GD} + \beta^i_H, \tag{3.9}$$

where β^i_{GD} denotes a "$\bar{\Gamma}$-driver" component, and β^i_H a "horizon component" that will be responsible for moving the horizon to a desired location.

We choose the $\bar{\Gamma}$-driver shift β^i_{GD} to satisfy the set of equations

$$\begin{aligned} \partial_t \beta^i_{GD} &= \frac{3}{4} B^i \,, \\ \partial_t B^i &= \partial_t \bar{\Gamma}^i_{GD} - \eta B^i \end{aligned} \tag{3.10}$$

where $\partial_t \bar{\Gamma}^i_{GD}$ is computed like $\partial_t \bar{\Gamma}^i$, but using the $\bar{\Gamma}$-driver component of the shift, β^i_{GD} alone. To motivate this choice, we note that the $\bar{\Gamma}$-driver shift condition allows evolutions of black holes to settle down into stationary trumpet solutions[9]. For these stationary solutions all time-derivatives vanish,

in particular we have $\partial_t \bar{\Gamma}^i = 0$, which implies from Eq[2.32]

$$\begin{aligned} -2\tilde{A}^{ij}\partial_j\alpha + 2\alpha\left(\bar{\Gamma}^i_{jk}\tilde{A}^{kj} - \frac{2}{3}\bar{\gamma}^{ij}\partial_j K + 6\tilde{A}^{ij}\partial_j ln\psi\right) + \beta^j\partial_j\bar{\Gamma}^i \\ - \bar{\Gamma}^j\partial_j\beta^i + \frac{2}{3}\bar{\Gamma}^i\partial_j\beta^j + \frac{1}{3}\bar{\gamma}^{li}\partial_l\partial_j\beta^j + \bar{\gamma}^{lj}\partial_j\partial_l\beta^i = 0 \end{aligned} \tag{3.11}$$

Now if we had chosen to evaluate $\partial_t\bar{\Gamma}^i$ in Eq[3.10] using the complete shift β^i, the evolution would then settle down to a stationary solution for the shift β^i satisfying Eq.[3.11], no matter how we decompose the shift in Eq.[3.9]. By evaluating $\partial_t\bar{\Gamma}^i$ from the $\bar{\Gamma}$-driver component β^i_{GD} alone, on the other hand, it is only this component that is driven into a stationary state, and we can still add a horizon shift β^i_H. In the evolution equations themselves, we still evaluate all right-hand sides using the complete shift β^i.

Constructing β^i_H:

The desired horizon location is described as a level-surface as in Eq.[3.7]. The function $h(\theta,\phi)$ measures the coordinate distance from the center (corresponding to r = 0) of the black hole. On the actual apparent horizon, given by h_{AH}, we have $\Theta(h_{AH}) = 0$, but, as long as the horizon is not yet at its desired location h, we have $\Theta(h) \neq 0$. At least in spherical symmetry, Θ is positive if the coordinate location h is outside of the apparent horizon, i.e. $h > h_{AH}$. In this case we want the shift to be pointing towards the center, so that coordinate observers move inwards. This means that the coordinate label of the horizon will increase. Exactly the opposite is true if h is inside the apparent horizon, at least for sufficiently small distances inside the horizon or for black holes with a sufficiently simple structure. These considerations suggest the choice,

$$\beta^i_H = f(r)\; A\; (h_{AH} - h)\; s^i \tag{3.12}$$

where $f(r) = \left(\frac{r}{1+r^2}\right)$ is a function that ensures $\beta^i_H = 0$ both at the center and at infinity, and A is an overall scale factor in the function $f(r)$ that shows how "strong" this function is, and how "fast" it makes the horizon move. The "width" of this function determines the size of the area in which grid points are moved. Other choices for $f(r)$ are also possible. Once the coordinates have been moved

around so that the apparent horizon is located at h, we have $\Theta(h) = 0$, and also $\beta^i_H = 0$.

3.4 Results and Discussion

Here we show some results from evolving the maximally-sliced trumpet data after implementing the horizon-shifting $\bar{\Gamma}$-driver condition as discussed above. The AHF module now takes in the user defined quantities **bssn_ rah0**, which is the desired location of the horizon and **bssn_ rahA** that defines the amplitude A in Eq.[3.12].

• **bssn_ rah0 = 0.89; bssn_ rahA = 0 :** This case should give us results when $\beta^i_H = 0$ i.e. the standard evolution, without any "horizon-stretching".

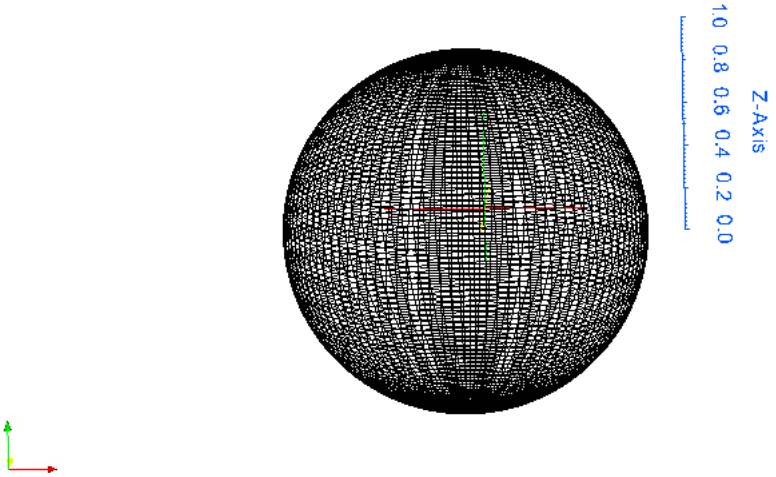

(a) The horizon at $r = 0.83M$ given by AHF

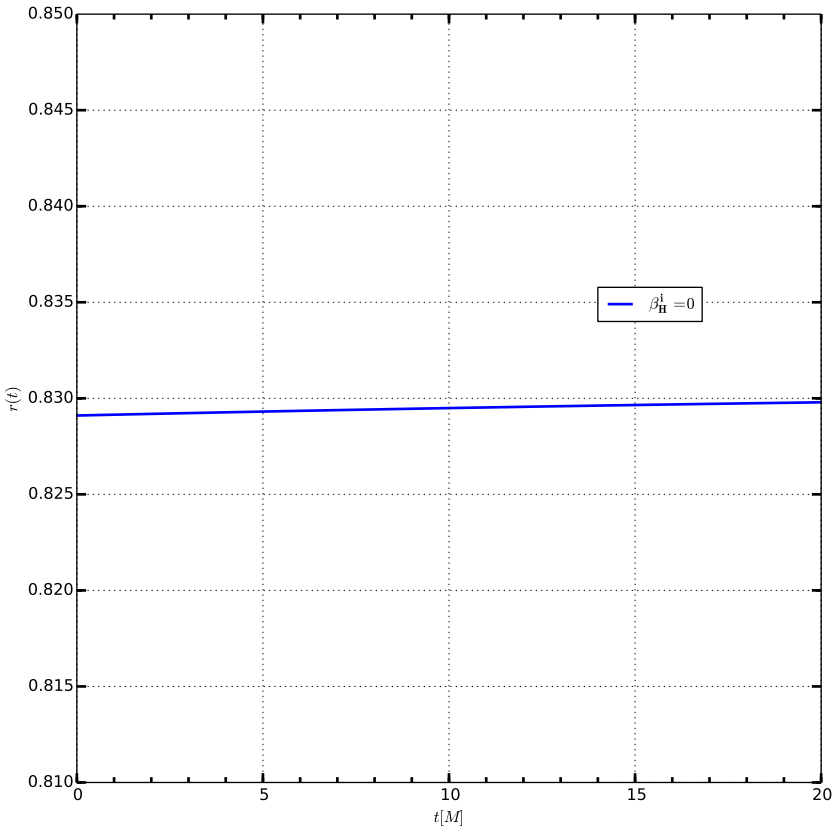

(b) Horizon w.r.t time

Figure 3.2: Evolution for $\beta^i_H = 0$

• **bssn_ rah0 = 0.89; bssn_ rahA = 0.5 :** In this case the horizon is “stretched” so that the coordinate size of the Schwarzschild black hole is increased to 0.89M

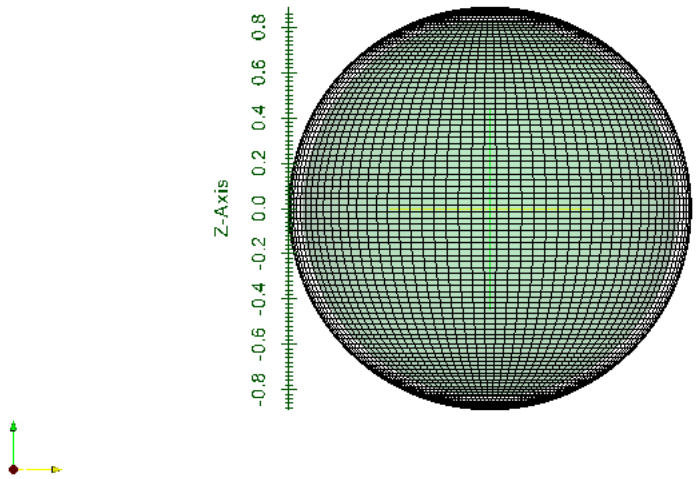

(a) The ‘solid’ horizon at $r = 0.83M$ is from $\beta^i_H = 0$ and the ‘wireframe’ horizon at $r = 0.89M$ is the “stretched” horizon

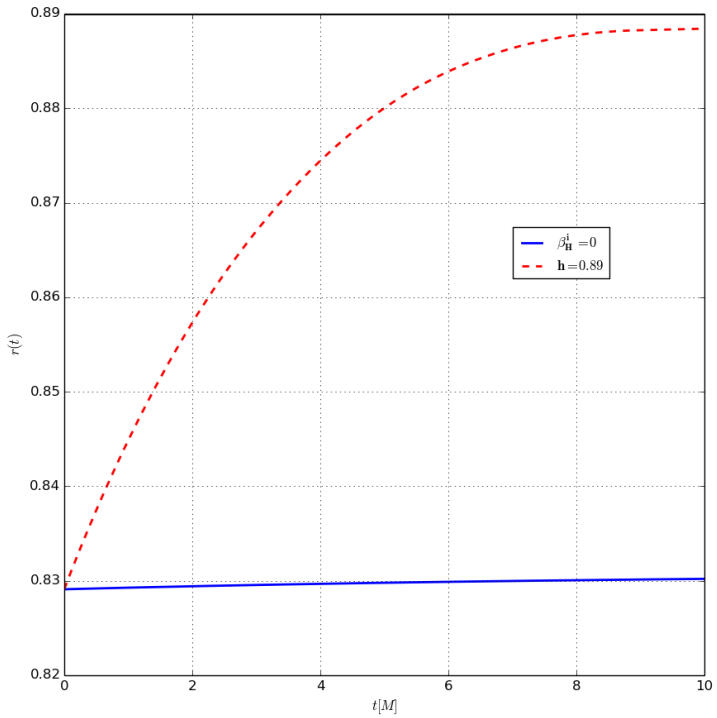

(b) Horizon w.r.t time

Figure 3.3: Evolution for $h = 0.89M$

• **bssn_ rah0 = 0.6; bssn_ rahA = 0.5 :** In this case the horizon is “shrunk” so that the coordinate size of the Schwarzschild black hole is decreased ≈ 0.6M

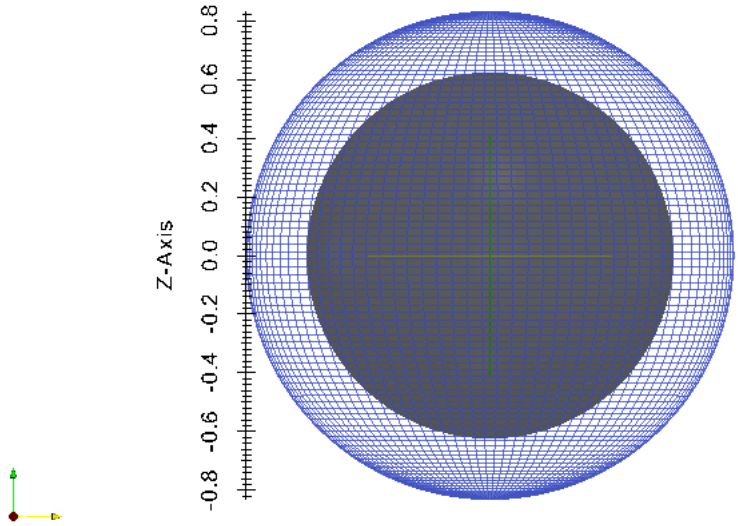

(a) The ‘wireframe’ horizon at $r = 0.83M$ is from $\beta^i_H = 0$ and the ‘solid’ horizon at $r \sim 0.6M$ is the “shrunk” horizon

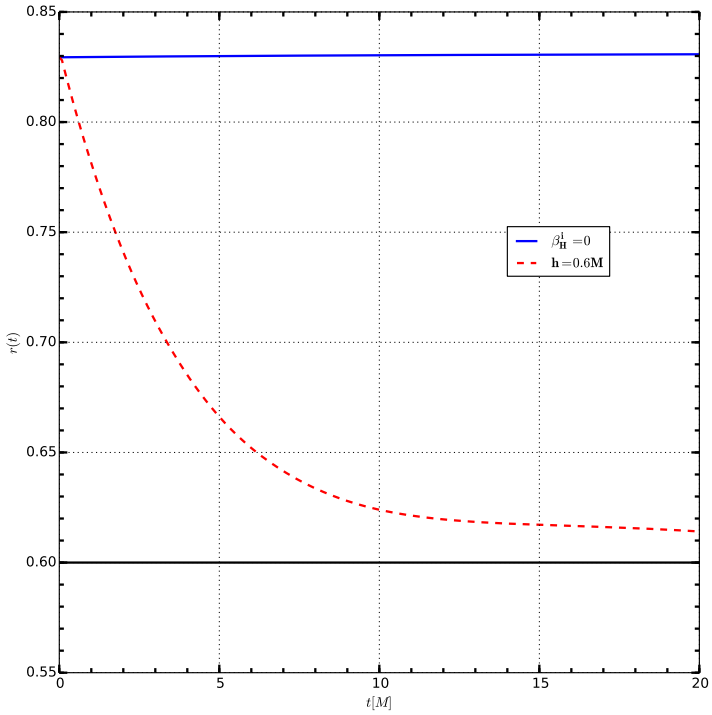

(b) Horizon w.r.t time

Figure 3.4: Evolution for $h = 0.6M$

The surface of the apparent horizon is outputted by the AHF module in the form of UnstructuredGridCells. We used 'ParaView'-viewer to visualize the surface and also make animation of the horizon shift. As can be seen from the plots of $r(t)$ Vs. $t[M]$, our approach does 'shift' the horizon to the desired location. Initially when the horizon is far from the desired location, the rate at which the horizon-shift occurs is large as compared to when it has reached close to the desired location. This is seen in both the cases where the horizon is moved. This feature is crucial for stable evolutions for longer times. But again in simulations running for longer times it has been seen that the errors from the boundary propagate into the inner grids and this may make the horizon-shifting unstable.

In order to verify that we did not introduce any errors in the evolution we perform the convergence test for the modified BAM code. The code should still be fourth-order convergent at least upto x =100M as discussed earlier in section[2.7.1]. For this convergence test we used the Hamiltonian constraint only in the x-direction due to the symmetry.

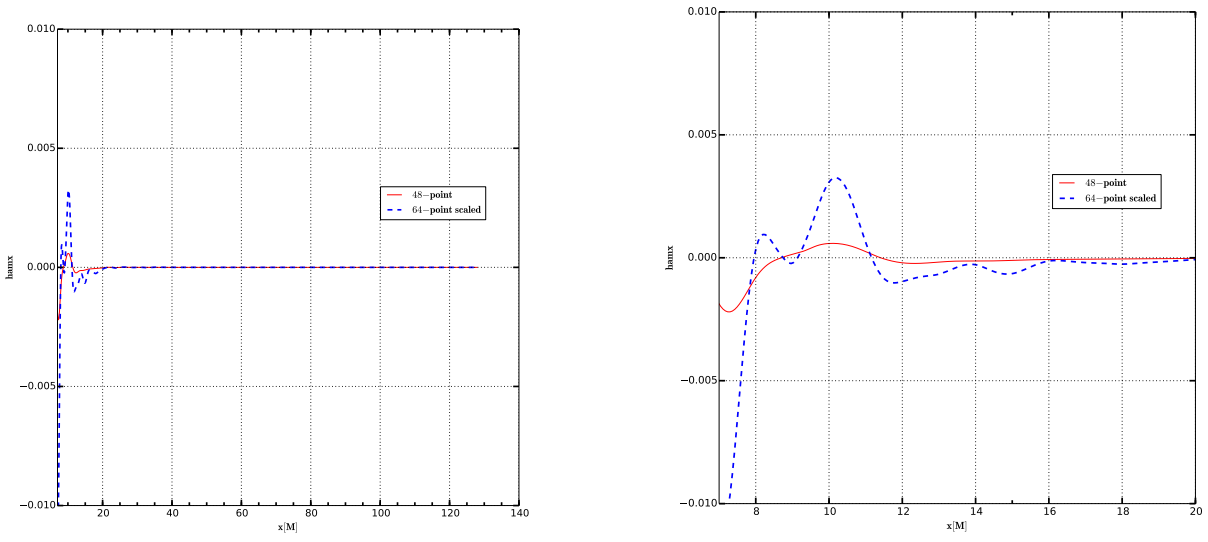

(a) full range of x

(b) near the puncture

Figure 3.5: The Hamiltonian constraint in the x-direction after 20M of evolution of the time-independent trumpet puncture data using the horizon adjusting shift. The Hamiltonian constraint at two resolutions (48 and 64-point) are scaled assuming fourth-order convergence, and we do see that the errors converge to zero at fourth-order. Near the puncture we don't expect to see convergence as this region requires much higher resolution than we used in this thesis.

Another verification would be to see if we were actually solving the Einstein's equation for the

vacuum spacetime. To see this we plot the norm of the Hamiltonian over the evolution. In vacuum spacetime the norm of the Hamiltonian should go to zero as we increase the resolution and this can be seen from Figure[3.6].

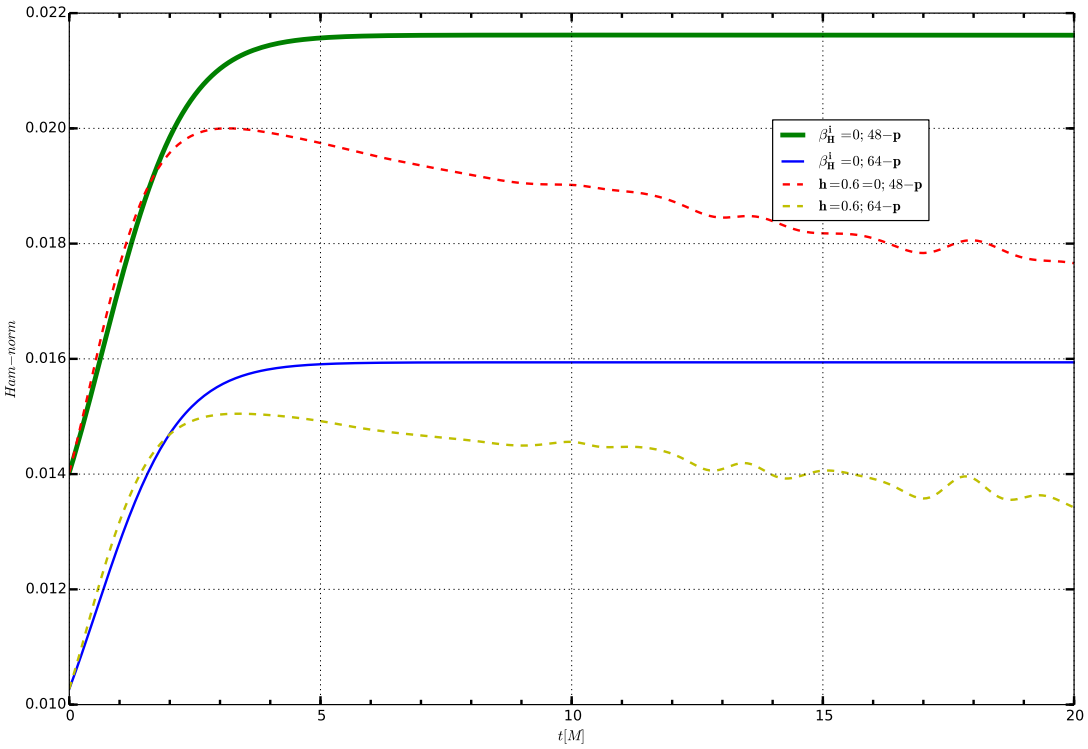

Figure 3.6: The thick solid line at the top and the dashed line originating from it are from the 48-point run for $\beta^i_H = 0$ and $h = 0.6M$ cases respectively. Similarly, the lines at the bottom are from the 64-point run.

For the horizon-"stretching" case, Fig.[3.3], we see that the Hamiltonian constraint is not satisfied. In Fig.[3.7] we see that as we increase the resolution the Hamiltonian norm for the higher resolution (64-point grid) is more than the one for the lower resolution (48-point grid). This shows that there is no convergence as we increase the resolution. If there was convergence we would have seen that on increasing the resolution the Hamiltonian norm would have gone to zero and would have been exactly zero (since vacuum spacetime) for infinite resolution. This suggests that there is some bug in the code that introduces some error which propagates over the evolution and makes the horizon-"shifting" unstable. Fig.[3.8] shows the Hamiltonian norm for t=4M evolution and clearly we see that the errors have accumulated around 2M of the evolution and we don't see any convergence after that. Errors

are propagated faster with higher resolution than the lower one and this is seen in Fig.[3.8] where the 64-point resolution evolution is contaminated earlier than the 48-point resolution run.

For the case of horizon "shrinking" we showed in Fig.[3.6] that the code was still convergent but that may have been due to shorter time for evolution. For longer evolutions it would turn out that the code looses convergence. The results indicate that the method works in principle, but since the constraints do not converge to zero, there must be some small inconsistency on the implementation of the horizon-shifting method, that introduces non-physical errors that spoil the simulation after $\sim$20M of evolution.

We were successful in showing that our idea of rescaling the coordinate size of the black holes worked, at least for the shorter evolutions that we performed. We believe that this will work even for loner evolutions as intended If the inconsistency in implementation can be identified. We showed through convergence argument that the evolutions are becoming unstable due to errors propagating in the data due to possible errors that we may have introduced in the BAM code while modifying it or otherwise.

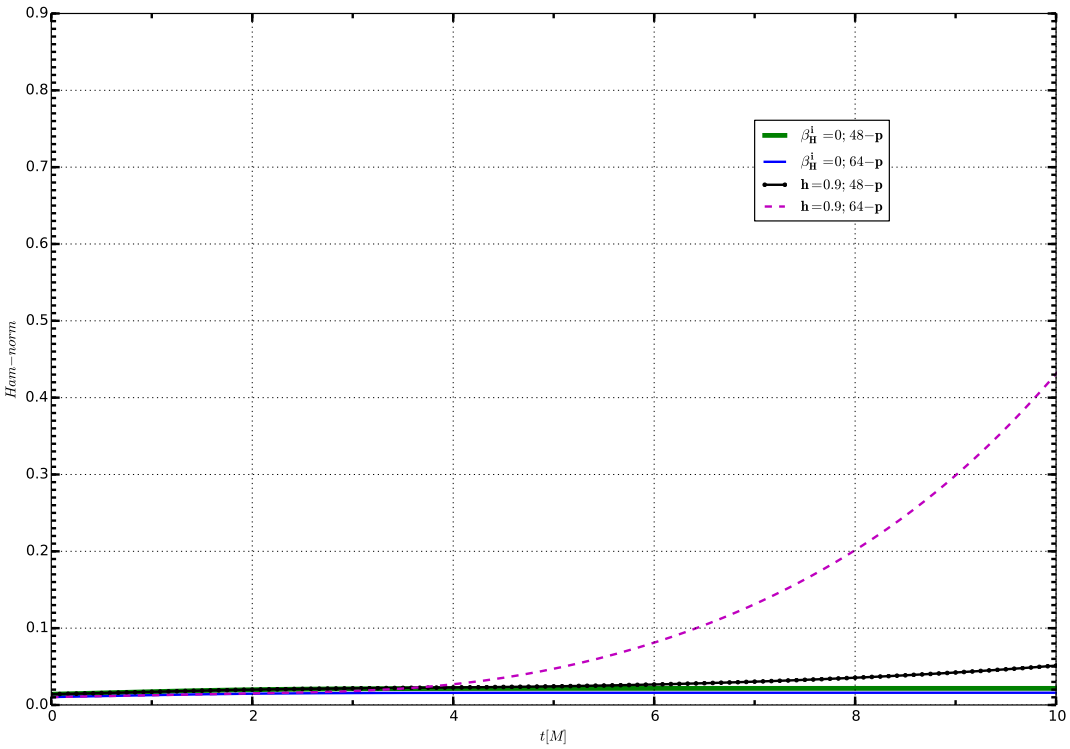

Figure 3.7: The norm of the Hamiltonian from the horizon-"stretching" case.

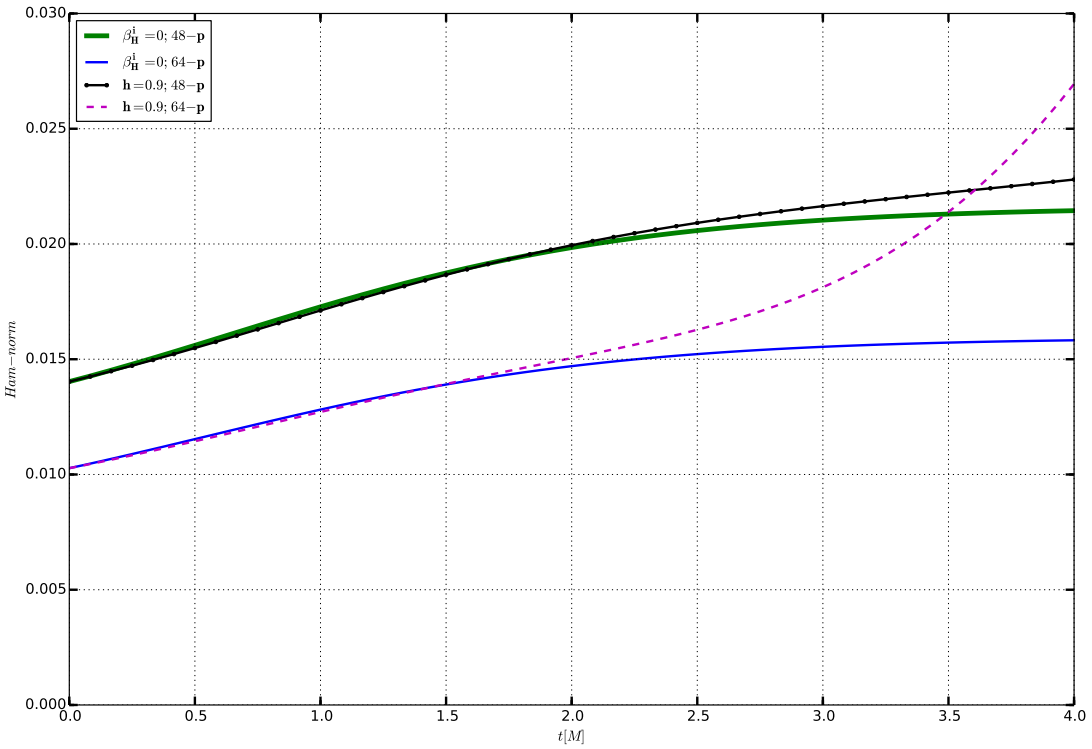

Figure 3.8: Zoomed-in version for Fig.[3.7]

Chapter 4

Conclusion and Future Direction

We began by briefly reviewing GR and gravitational waves which give the motivation to do Numerical Relativity (NR). We reviewed the derivation for 3+1 decomposition of the Einstein's equations thereby introducing concepts important in NR. We then laid out the BSSN-formalism which is the workhorse for the "moving-puncture" approach for numerically solving the Einstein's equations. Having reviewed the necessary casting of the field equations in 3+1 form, we present some aspects of solving the initial data problem, the gauge conditions used and a note on discretizing the field equation's and thereby relating all this to our work in this thesis.

A convergence test is an invaluable tool in validating the accuracy of a code. It can report sources of error introduced in the code i.e., if the errors come from inconsistent implementation in the code or due to discretization of the quantities. If the errors were due to discretization then on increasing the resolution these errors would go to zero and become zero for infinite resolution. On the other hand this would not be the case if the errors were introduced from inconsistent implementation in the code. In this thesis we verified the convergence results for the BAM code which solves the BSSN form of the Einstein's equations in 3D Cartesian coordinates. It is a fully general relativistic finite-difference code that is capable of simulating multiple black holes before and through merger. From the convergence test we were also able to verify that the 'trumpet' initial data that were used in this work are indeed time-independent.

We discussed the concept of apparent horizons and their importance as a diagnostic tool in numer-

ical evolutions of the Einstein's equations. We also reviewed the derivation of the equation governing the location of apparent horizon and how they are solved numerically, mainly focusing on the 'flow'-algorithm that the BAM code uses to locate the horizon. We presented our ansatz of "shifting" the horizon and its implementation in the BAM code. We showed promising results from our implementation of the horizon-"shifting" ansatz. We showed that the coordinate size of a black hole can be shifted to a given desired location. From convergence tests we identified the possible existence of an error in the code that contaminated long term evolution and made the horizon-shifting unstable. To fix this we would require a detailed check of all aspects of the modification of the BSSN evolution code to identify and remove the error, and to then show that long term stable evolution with horizon-"shifting" shift vector is possible. It'll be a humongous task fixing the code and will require some time. Nonetheless, our initial results indicate that this is a promising approach to dynamically control the horizon size (and therefore resolution requirements) of moving-puncture codes.

For future work a detailed study of implementing the horizon-"shifting" ansatz to black hole binaries and the degree to which it relaxes the resolution requirements can be carried out.

Bibliography

[1] J. H. Taylor and J. M. Weisberg.“ A new test of general relativity: Gravitational radiation and the binary pulsar PSR 1913+16”. Astrophysical Journal, 253:908-920, 1982.

[2] A. A. Abramovici, W. Althouse, R. P. Drever, Y. Gursel, S. Kawamura, F. Raab, D. Shoemaker, L. Sievers, R. Spero, K. S. Thorne, R. Vogt, R. Weiss, S. Whitcomb, and M. Zuker. “LIGO: The Laser Interferometer Gravitational-wave Observatory. Science”, 256:325-333, 1992.

[3] E. E. Flanagan and S. A. Hughes. “Measuring gravitational waves from binary black hole coalescence: I. Signal to noise for inspiral, merger, and ringdown”. gr-qc, 9701039, 1997. Submitted to Physical Review D.

[4] Albert Einstein: Über Gravitationswellen. *Sitzungsberichte der Königlich Preußischen Akademie der Wissenschaften (Berlin)*, pp. 154-167, 1918.

[5] H. Bondi, M.G.J. van der Burg, and A.W.K. Metzner., “Gravitational waves in general relativity. VII. Waves from axisymmetric isolated systems”. *Proc.Roy.Soc.Lond.,* A269:21-52, 1962.

[6] R.K. Sachs., “Gravitational waves in general relativity. VIII. Waves in asymptotically flat space-times”. *Proc.Roy.Soc.Lond.,* A270:103-126, 1962

[7] “Numerical Relativity: Solving Einstein’s Equations on the Computer”, ISBN: 9780521514071

[8] Cook, G. B., “Initial Data for Numerical Relativity”, Living Rev. Relativity, 3, lrr-2000-5 (2000).

[9] Mark Hannam, Sascha Husa, Frank Ohme, Bernd Brügmann, and Niall Ó Murchadha.,

"Wormholes and trumpets: the Schwarzschild spacetime for the moving-puncture generation", Phys.Rev.D78:064020,2008

[10] Smarr, L. and York Jr, J. W., "Kinematical conditions in the construction of spacetime", Phys. Rev. D, 17, 2529-2551 (1978)

[11] Estabrook, F., Wahlquist, H., Christensen, S., DeWitt, B., Smarr, L. et al., "Maximally slicing a black hole", Phys. Rev. D, 7, 2814-2817 (1973).

[12] Bona, C., Massó, J., Seidel, E. and Stela, J., "A New Formalism for Numerical Relativity", Phys. Rev. Lett., 75, 600-603 (1995).

[13] Thornburg, J., "Coordinates and boundary conditions for the general relativistic initial data problem", Class. Quantum Grav., 4, 1119-1131 (1987).

[14] Diener, P., "A new general purpose event horizon finder for 3-D numerical spacetimes", Class. Quantum Grav., 20, 4901-4918 (2003)

[15] Cohen, M. I., Pfeiffer, H. P. and Scheel, M. A., "Revisiting Event Horizon Finders", Class. Quantum Grav., 26, 035005 (2009).

[16] Robert M. Wald and Vivek Iyer. "Trapped surfaces in the Schwarzschild geometry and cosmic censorship". Phys. Rev. D, 44:R3719-R3722, 1991.

[17] Thornburg, J., "Event and Apparent Horizon Finders in 3+1 Numerical Relativity", Living Rev. Relativity, 10, lrr-2007-3 (2007).

[18] Carsten Gundlach. "Pseudo-spectral apparent horizon finders: an efficient new algorithm". Phys. Rev. D, 57:863-875, 1998.

[19] Takashi Nakamura, Yasufumi Kojima, and Ken-ichi Oohara. "A method of determining apparent horizons in three-dimensional numerical relativity". Phys. Lett. A, 106(5-6):235-238, 10 December 1984.

[20] Miguel Alcubierre, S. R. Brandt, B. Brügmann, C. Gundlach, Joan Masśo, E. Seidel, and P. Walker.“ Test-beds and applications for apparent horizon finders in numerical relativity”. Class. Quantum Grav., 17:2159-2190, 2000.

[21] C. W. Misner, K. S. Thorne ans J.A. Wheeler, Gravitation (W. H. Freeman and sons 1973)

[22] James B. Hartle, Gravity: An Introduction to EinsteinâĂŹs General Relativity, Addison Wesley(2003)